Wake transition of an unconstrained self-propelled flexible flapping plate

Kui Liu and Haibo Huang*

Department of Modern Mechanics, University of Science and Technology of China, Hefei, Anhui 230026, People's Republic of China

(Received 18 September 2023; accepted 6 March 2024; published 21 March 2024)

This paper numerically investigates the wake transition of an unconstrained self-propelled flexible flapping plate, which exhibits the ability to move freely both longitudinally and laterally, at a low Reynolds number of 200. By examining crucial parameters, including pitching amplitude θ_0, bending stiffness K, and mass ratio of the plate to the fluid M, the research identifies three distinct wake patterns: symmetric, deflected, and chaotic. The lateral drift speed of the plate (V) is used as a quantitative indicator to differentiate between symmetric and asymmetric wake patterns, where V is approximately zero and nonzero, respectively. The paper indicates that the transition from symmetric to asymmetric wakes occurs when the cruising Reynolds number (Re_c) reaches the critical value ($\mathrm{Re}_c^{\mathrm{cr}}$), which follows a simple scaling law vs M, i.e., $\mathrm{Re}_c^{\mathrm{cr}} \sim M^{-1/2}$. The critical dimensionless translational kinetic energy $\hat{E}_k$ of the plate remains constant for various M when the wake transition occurs. Analyzing translational kinetic energy not only proves the $\mathrm{Re}_c^{\mathrm{cr}}$ scaling, but also offers a unique energy perspective on the phenomenon. In addition, the critical flapping Reynolds number ($\mathrm{Re}_f^{\mathrm{cr}}$) is found to also satisfy a simple scaling similar to $\mathrm{Re}_c^{\mathrm{cr}}$, i.e., $\mathrm{Re}_f^{\mathrm{cr}} \sim M^{-1/3}$. Finally, it is revealed that passive lateral oscillation and bending deformation of the plate are two key mechanisms affecting wake symmetry properties. This paper provides insights into flapping-based locomotion.

DOI: 10.1103/PhysRevFluids.9.033102

I. INTRODUCTION

Flapping systems, such as swimming fish and flying birds or insects, use fins or wings to generate thrust for locomotion in nature. The desire to deepen our understanding of the biology of these creatures and to offer insights for bionic design has sparked significant interest in flapping-based locomotion over the past few decades [1,2]. Numerous experimental, theoretical, and numerical studies on this topic can be found in the literature. Some physical mechanisms underlying flapping-based propulsion have been addressed by researchers [3,4].

Recent studies have placed particular emphasis on investigating wake patterns and transitions in flapping systems [5–7]. A wake is formed when a flapping body oscillates in an oncoming flow or self-propels in a stationary fluid, leaving behind a pattern similar to footprints made by terrestrial animals on the ground [8]. The characteristics of these wakes are intricately linked to the performance of the flapping body [9]. However, note that swimming performance cannot be analyzed solely through wake structures, since it may fail under some circumstances [10].

Previous investigations [7,11–15] have identified various wake patterns under different parameters. When the amplitude-based Strouhal number $\mathrm{St}_A = 2Af/U$ (where U is the inflow speed, and A and f are the oscillation amplitude and frequency, respectively) is small, a classical Bénard–von Kármán (BvK) vortex street is formed. The corresponding mean flow profile is similar to that

*huanghb@ustc.edu.cn

 ©2024 American Physical Society

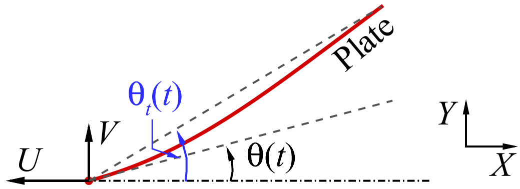

FIG. 1. Schematic diagram of an unconstrained pitching flexible plate. The plate can move freely in both x and y directions. Here, $\theta(t)$ and $\theta_t(t)$ represent the instantaneous pitching angle of the leading and trailing edges, respectively, U and V denote the horizontal and vertical velocities of the plate, respectively.

behind drag-producing bodies, meaning that the BvK wake is a drag wake [8]. At higher St_A, i.e., at higher transverse oscillation speeds, the reversed Bénard–von Kármán (rBvK) vortex street is observed, in which the vorticity sign of each vortex is reversed compared to the BvK vortex street. In this configuration, the mean flow has the form of a jet. Hence, the rBvK wake is often seen as a predictor of thrust generation. However, generating a net thrust requires a relatively large St_A since the transition from a BvK wake to an rBvK wake occurs before the drag-thrust transition [6,7,13]. Further increasing St_A triggers symmetry breaking of the rBvK wake and results in a deflected wake [7,13–15]. For a flexible body with higher St_A, a chaotic wake (more asymmetric compared to the deflected wake) may be observed [7]. More complex wake structures, e.g., $2P$ (two vortex pairs) wakes, are also possible [5].

In the aforementioned studies, the plates or foils are tethered in an oncoming flow. However, a crucial distinction arises for self-propelled bodies, as the BvK wake is not expected to form due to the need for thrust to propel the body forward. In such cases, wake transitions primarily involve symmetric and asymmetric rBvK wakes. Zhu *et al.* [16] numerically studied the wake symmetry properties of a self-propelled flexible plate and noted that plate flexibility primarily affects vortex circulation modification, subsequently affecting wake symmetry properties. It is worth noting, though, that the plate in Zhu *et al.* [16] possessed self-propulsion capabilities solely in the longitudinal direction, while natural flapping systems exhibit multidirectional motion. On the other hand, Lin *et al.* [17] did not observe any symmetry breaking of the rBvK wake in unconstrained flapping foils, possibly due to their rigid foil. Given that flexibility has a substantial impact on both the propulsion performance and flow structures of plates or foils [15,16,18–20], unresolved issues persist concerning the wake symmetry properties of unconstrained flexible bodies, warranting further investigation.

This paper employs numerical methods to investigate wake patterns in self-propelled flexible plates. The plate is capable of unrestricted movement in both the longitudinal and lateral directions, enabling a dynamic response to the surrounding flow. We examine how variations in bending stiffness, pitching amplitude, and the plate-to-fluid mass ratio impact wake patterns and plate performance. Our primary focus lies in elucidating potential correlations between wake transitions and the performance metrics of the plates, such as cruising speed and kinetic energy, with the aim of providing a sound physical rationale.

The rest of this paper is organized as follows. The physical problem and mathematical formulation are given in Sec. II. The numerical method and validation are described in Sec. III. Detailed results are discussed in Sec. IV and concluding remarks are addressed in Sec. V.

II. PHYSICAL PROBLEM AND MATHEMATICAL FORMULATION

The schematic diagram of the unconstrained pitching flexible plate that we considered is shown in Fig. 1. In this configuration, the leading edge of the plate undergoes forced pitching. The mathematical representation of this movement can be expressed as follows:

$$\theta(t) = \theta_0 \sin(2\pi f t), \tag{1}$$

where $\theta(t)$ denotes the instantaneous pitching angle, θ_0 represents the pitching amplitude, and f signifies the flapping frequency. It is worth emphasizing that, in contrast to prior studies like Zhu *et al.* [16] and Liu *et al.* [21], the plate investigated in our current paper possesses the capability to move unrestrictedly in both the x and y directions, facilitated by fluid-structure interaction. Consequently, even in the absence of deliberate heaving motion, the plate has the potential to passively exhibit lateral heaving.

We employ the incompressible Navier-Stokes equations to model and solve the fluid flow:

$$\frac{\partial \boldsymbol{v}}{\partial t} + \boldsymbol{v} \cdot \nabla \boldsymbol{v} = -\frac{1}{\rho}\nabla p + \frac{\mu}{\rho}\nabla^2 \boldsymbol{v} + \boldsymbol{f}_b, \tag{2}$$

$$\nabla \cdot \boldsymbol{v} = 0, \tag{3}$$

where $\boldsymbol{v}$ is the velocity, p is the pressure, ρ is the density of the fluid, μ is the dynamic viscosity, and $\boldsymbol{f}_b$ denotes the Eulerian force density [16] acting on the surrounding fluid due to the immersed boundary.

The structural equation is employed to describe the deformation and motion of the plate [22–24]:

$$\rho_l \frac{\partial^2 \boldsymbol{X}}{\partial t^2} - \frac{\partial}{\partial s}\left[Eh\left(1 - \left|\frac{\partial \boldsymbol{X}}{\partial s}\right|^{-1}\right)\frac{\partial \boldsymbol{X}}{\partial s}\right] + EI\frac{\partial^4 \boldsymbol{X}}{\partial s^4} = \boldsymbol{F}_s, \tag{4}$$

where s is the Lagrangian coordinate along the plate, ρ_l is the structural linear mass density, $\boldsymbol{X}(s,t) = (X(s,t), Y(s,t))$ is the position vector of the plate, and $\boldsymbol{F}_s$ is the Lagrangian force per unit length exerted on the plate by the surrounding fluid. Eh and EI denote the structural stretching rigidity and bending rigidity, respectively. At the leading edge of the plate, the boundary conditions are expressed as

$$-Eh\left(1 - \left|\frac{\partial \boldsymbol{X}}{\partial s}\right|^{-1}\right)\frac{\partial \boldsymbol{X}}{\partial s} + EI\frac{\partial^3 \boldsymbol{X}}{\partial s^3} = 0, \quad \frac{\partial \boldsymbol{X}}{\partial s} = (\cos\theta, \sin\theta). \tag{5}$$

Note that the first boundary condition in (5) represents the horizontally and vertically unconstrained condition, and the second boundary condition represents the lateral pitching motion. At the free end, the internal force and bending moment are zero. Hence the boundary conditions are

$$-Eh\left(1 - \left|\frac{\partial \boldsymbol{X}}{\partial s}\right|^{-1}\right)\frac{\partial \boldsymbol{X}}{\partial s} + EI\frac{\partial^3 \boldsymbol{X}}{\partial s^3} = 0, \quad \frac{\partial^2 \boldsymbol{X}}{\partial s^2} = 0. \tag{6}$$

In our paper, the fluid density ρ, the dimensional length of the plate L (= 1), and characteristic velocity $U_{\mathrm{ref}} = fL$ are chosen to normalize the above equations. Therefore, the characteristic time is $T_{\mathrm{ref}} = L/U_{\mathrm{ref}}$. Based on dimensional analysis, the following dimensionless governing parameters are introduced: the pitching amplitude θ_0, the Reynolds number $\mathrm{Re} = \rho U_{\mathrm{ref}} L/\mu$, the mass ratio of the plate to the fluid $M = \rho_l/\rho L$ (note that in the context of our two-dimensional case, considering unit depth, the comprehensive definition of the dimensionless parameter M is expressed as $M = \frac{\rho_l}{\rho L \cdot 1} = \frac{\rho_l}{\rho L}$), the stretching stiffness $S = Eh/\rho U_{\mathrm{ref}}^2 L$, and the bending stiffness $K = EI/\rho U_{\mathrm{ref}}^2 L^3$.

III. NUMERICAL METHOD AND VALIDATION

The lattice Boltzmann method [24] is used to solve the Navier-Stokes equations numerically, while a finite element method is employed to solve for the motion of the flexible plate [25]. The immersed boundary method [22] is utilized to couple the fluid and structure solvers. To enforce the no-slip boundary condition, the body force term $\boldsymbol{f}_b$ in (2) is included as an interaction force between the fluid and the immersed boundary. The deformation of the plate is handled using the corotational scheme [25], which is capable of handling large displacements. More details on numerical methods can be found in our previous papers [24,26,27].

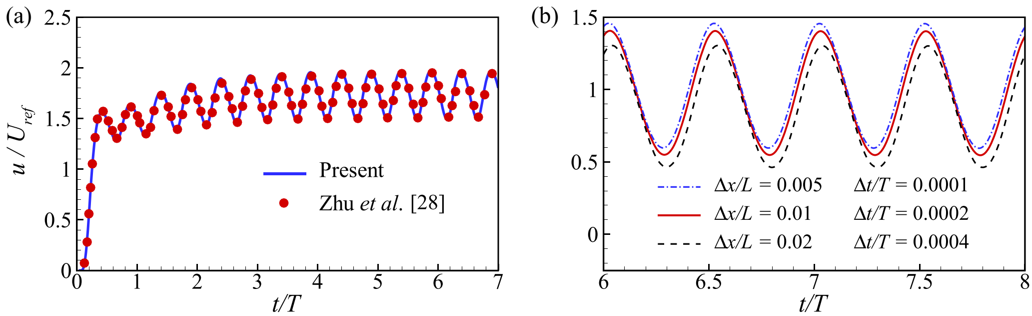

FIG. 2. (a) The streamwise velocity of the leading edge as a function of time in the case of a self-propelled heaving plate with the nondimensional governing parameters: $\mathrm{Re} = 200$, $h_0 = 0.5$, $M = 0.2$, $K = 0.8$ and $S = 1000$ [28]. This is a constrained case. The plate is equipped with self-propulsion capabilities exclusively in the longitudinal direction. (b) Grid independence and time-step independence studies for an unconstrained self-propelled plate with $K = 1$, $M = 0.2$, and $\theta_0 = 25^\circ$.

The simulations are conducted on a computational domain of size $[-15, 25] \times [-15, 15]$ in x and y directions, which is large enough to eliminate any boundary effects. The boundaries are subject to a constant pressure with $\boldsymbol{v} = 0$, except at the outlet where a constant pressure is imposed with $\partial \boldsymbol{v}/\partial x = 0$. Initially, the velocity field of the fluid is zero throughout the domain. The mesh in the x and y directions is uniform with spacing $\Delta x = \Delta y = 0.01L$. The time step is $\Delta t = T/5000$ in our simulations of fluid flow and plate deformation, where $T = 1/f$ is the flapping period. Furthermore, a finite moving computational domain is used in the x direction to allow the plate to move for a sufficiently long time [24]. Upon the plate traveling one lattice in the x direction, the computational domain shifts, adding a layer at the inlet and removing one at the outlet.

To validate the numerical method, a single plate in isolated swimming [28] was simulated with $\mathrm{Re} = 200$, $h_0 = 0.5$, $M = 0.2$, $K = 0.8$, and $S = 1000$, where h_0 is the heaving amplitude. It is noted that the solver of Zhu *et al.* [28] uses the discrete stream-function formulation for the incompressible Navier-Stokes equations and a staggered finite difference method for the structural equation, which is completely different from ours. Figure 2(a) shows the streamwise velocity of the leading edge as a function of time. It is seen that the present result agrees well with that of Zhu *et al.* [28]. In addition, our numerical strategy has been validated and employed successfully to study many flow problems, including tandem flexible inverted flags in a uniform flow [26], the effect of trailing edge shape on the self-propulsive performance of heaving flexible plates [27], and the scaling laws of the self-propulsive performance of flexible plates [21]. Detailed numerical validations can also be found in these papers.

The results of grid independence and time-step independence for an unconstrained self-propelled plate with $K = 1$, $M = 0.2$, and $\theta_0 = 25^\circ$ are shown in Fig. 2(b). It is seen that the curve of $\Delta x/L = 0.01$ and $\Delta t/T = 0.0002$ is very close to that of $\Delta x/L = 0.005$ and $\Delta t/T = 0.0001$, with only a difference of no more than 5%, i.e., $\Delta x/L = 0.01$ and $\Delta t/T = 0.0002$ are sufficient to achieve accurate results. Hence, we use the mesh size and time-step size in our subsequent simulations.

IV. RESULTS AND DISCUSSION

In present simulations, the Reynolds number and stretching stiffness are fixed at $\mathrm{Re} = 200$ and $S = 1000$, respectively. Here S is large enough so that the plate is almost inextensible. The other key parameters are variable, i.e., the bending stiffness $K \in [0.2, 10]$, the pitching amplitude $\theta_0 \in [10^\circ, 40^\circ]$, and the mass ratio $M \in [0.2, 2]$. Note that the range of these parameters is consistent with previous studies and biological data [16,24,29–31]. For instance, the $\mathrm{Re} \sim O(10^2)$ is close to that of larvae [29] and θ_0 of many swimming or flying animals lies in the range $[14.5^\circ, 38.4^\circ]$ [30].

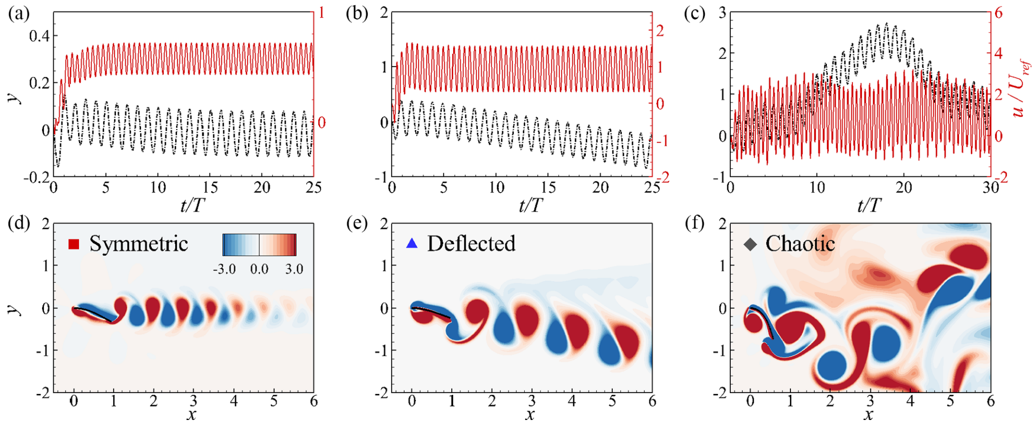

FIG. 3. Time histories of the lateral location y and streamwise velocity u of the leading edge of the plate (a)–(c) as well as instantaneous vorticity contours for the three typical cases with different wake patterns (d)–(f). The three columns correspond to different cases: (a) and (d) represent the symmetric-wake case with parameters $M = 0.2$, $\theta_0 = 25^\circ$, and $K = 0.4$; (b) and (e) depict the deflected-wake case with parameters $M = 0.2$, $\theta_0 = 30^\circ$, and $K = 2$; (c) and (f) illustrate the chaotic-wake case with parameters $M = 0.8$, $\theta_0 = 40^\circ$, and $K = 2$.

A. Wake transitions and scaling laws

First, we investigate how θ_0 and K affect the wake symmetry properties of the pitching plate under various M. Extensive simulations have revealed three predominant wake patterns: symmetric, deflected, and chaotic wakes. Figure 3 shows a typical example for each of these wake patterns.

In the case of $M = 0.2$, $\theta_0 = 25^\circ$, and $K = 0.4$ [see Fig. 3(a)], the plate reaches a stable state after approximately 15 flapping cycles. Here, both the lateral location of the leading edge (y) and the instantaneous streamwise velocity (u) oscillate around fixed values, indicating that the plate can self-propel in a straight line along the streamwise direction. In this situation, a symmetric reversed von Kármán vortex street, i.e., a symmetric wake, is generated behind the plate [see Fig. 3(d)].

In the case of $M = 0.2$, $\theta_0 = 30^\circ$, and $K = 2$ [see Fig. 3(b)], the plate continually drifts laterally while maintaining a stable propulsion speed after a few cycles. This indicates that the plate's propulsion trajectory is deflected, and we observe a deflected wake characterized by the formation of counter-rotating vortices that shed in a dipole structure [see Fig. 3(e)]. Actually, the deflected wake will result in a net lift [14], inducing the lateral drift motion of the plate.

For higher M and θ_0, such as $M = 0.8$, $\theta_0 = 40^\circ$, and $K = 2$ [see Fig. 3(f)], a chaotic wake might be observed. In this scenario, neither the propulsion speed nor the lateral position of the plate reaches a stable state [see Fig. 3(c)]. It is worth noting that both deflected and chaotic wakes belong to asymmetric wake patterns, and the deflected wakes are observed in previous experimental or numerical studies [7,13,15,16]. Actually, our two-dimensional flapping plate simulation corresponds to the three-dimensional scenario with an infinite aspect ratio. Conducting experiments under such circumstances is impractical. Although chaotic wakes are observed in our paper, these may be artifacts of the two-dimensionality simulated. Nonetheless, this paper is the first to discuss these scenarios in the context of unconstrained self-propelled flexible plates.

We will now examine the time-averaged propulsion speed U and lateral drift speed V of the plate. Here U and V are defined as

$$U = -\frac{1}{T}\int_{t'}^{t'+T}\left(\frac{\partial X}{\partial t}\bigg|_{s=0}\right)dt, \quad V = \left|\frac{1}{T}\int_{t'}^{t'+T}\left(\frac{\partial Y}{\partial t}\bigg|_{s=0}\right)dt\right|. \tag{7}$$

It is noted that the definition of V includes the absolute value symbol, i.e., $V \geqslant 0$. The direction in which the plate drifts, either upward or downward, actually depends on the initial strokes. However,

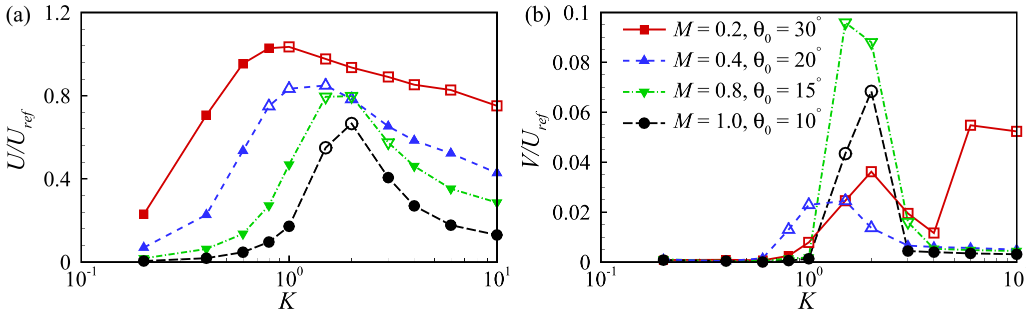

FIG. 4. (a) Propulsion speed U and (b) lateral drift speed V of the plate as functions of K for various M and θ_0. Solid and hollow symbols represent symmetric and asymmetric cases, respectively.

we have conducted tests with different phase angle, and found that the initial conditions have no effect on the wake symmetry properties, similar to the results in Ref. [16]. The flexible plate's U and V as functions of K for various M and θ_0 are shown in Fig. 4, where solid and hollow symbols represent symmetric and asymmetric cases, respectively. First, the figure reveals that U generally increases first and then decreases as K increases [see Fig. 4(a)], which is similar to that of a single directional self-propelled plate [32]. Therefore, for fixed M and θ_0, there exists an optimal stiffness K which maximizes the propulsive speed. This is because appropriate flexibility can enhance the thrust of the plate [15,33–35]. For symmetric wake patterns, V is almost zero ($V/U_{\text{ref}} < 0.01$), while the asymmetric ones exhibit significant V [see Fig. 4(b)]. Hence, monitoring V can serve as a valuable quantitative method for identifying wake patterns, complementing the direct observation of the flow field and the lateral location of the plate. While the wake symmetry can indeed be described by the deflection angle of the vortex street [14,36], observing V is a more convenient method, because it eliminates the need for additional processing of the flow field.

In addition, it can also be found that, except for cases with small M (i.e., $M = 0.2$), symmetric wakes are present in cases with smaller U [solid symbols in Fig. 4(a)]. In contrast, asymmetric wakes appear in cases with larger U [hollow symbols in Fig. 4(a)]. For example, for $M = 0.4$ and $\theta_0 = 20^\circ$ (blue dashed line in Fig. 4), the wake is symmetric if $U/U_{\text{ref}} < 0.7$; otherwise, the wake is asymmetric. This suggests that wake symmetry properties are related to the propulsion speed, which will be further analyzed in detail in the following discussions.

Further, the phase diagrams for the three wake patterns in the K-θ_0 plane for the unconstrained pitching plate with various M are presented in Fig. 5. It is seen that most cases with symmetric wake occur when K or θ_0 is small, i.e., the left or lower region of the phase diagram. However, as both K and θ_0 increase, symmetry breaking occurs within the symmetric wake, giving rise to asymmetric wakes, either deflected or chaotic. It is noteworthy that chaotic wakes are primarily found in cases with higher M, such as $M = 1$ and 2 [Figs. 5(e) and 5(f)]. This may be attributed to the occurrence of a more complex structural response when M is larger, as suggested by Ref. [16]. Moreover, the phase diagrams reveal that chaotic cases are encompassed by deflected cases, indicating a wake transition sequence from symmetric to deflected and then to chaotic as K and θ_0 gradually vary. However, considering the intricacies of chaotic wakes, our subsequent discussion on wake transitions focuses solely on symmetric and deflected wakes.

Our focus now shifts to quantitatively describing the boundaries separating symmetric and asymmetric regimes. Figure 5 reveals that these boundaries exhibit irregular shapes, making it challenging to provide concise and accurate descriptions solely through the parameters like K and θ_0. However, the analysis of Fig. 4 indicates a strong correlation between wake transition and propulsion speed. Consequently, we propose employing results, specifically the propulsion speed, rather than physical or motion parameters to delineate these boundaries more effectively. To achieve this, we introduce a cruising Reynolds number, denoted as $\text{Re}_c = |\boldsymbol{U}|L/\nu$. Here, U

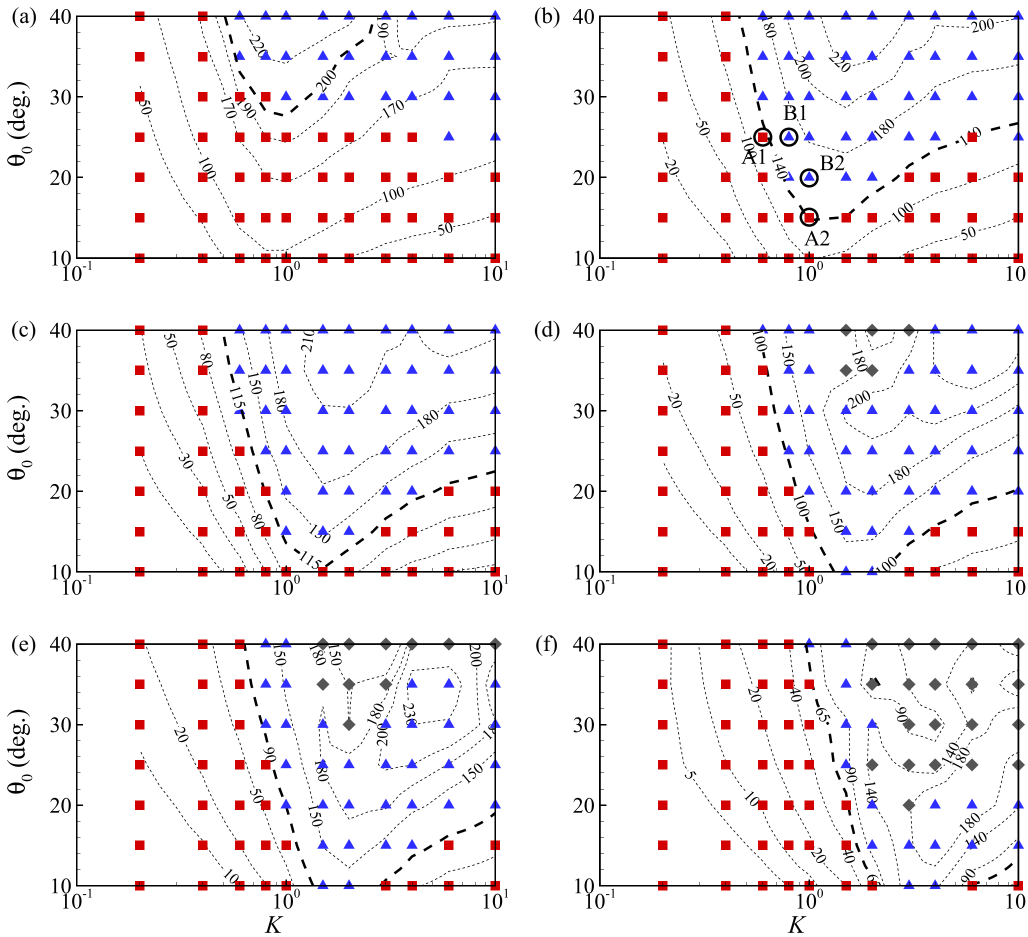

FIG. 5. Wake pattern regimes in the K-θ_0 plane for the unconstrained pitching plate with $M = 0.2$ (a), 0.4 (b), 0.6 (c), 0.8 (d), 1.0 (e), and 2.0 (f). The symbols □, △, and ♢ represent the symmetric, deflected, and chaotic wakes, respectively. Contours of the cruising Reynolds number Re_c are also presented. The thick dashed lines represent the critical cruising Reynolds number $\mathrm{Re}_c^{\mathrm{cr}}$, which separates the symmetric and asymmetric regimes. The marks A1, B1, A2, and B2 represent four typical cases close to the critical line, which will be discussed in detail in Fig. 6.

and V represent the x and y components of $\boldsymbol{U}$, respectively. Figure 5 presents contours of Re_c. Remarkably, it becomes evident that these boundaries align closely with specific contours. For instance, when considering various M such as $M = 0.4$, 0.6, 0.8, 1.0, and 2.0 [Figs. 5(b)–5(f)], contours for $\mathrm{Re}_c = 140$, 115, 100, 90, and 65 accurately correspond to the boundaries between symmetric and asymmetric regimes.

In the case of $M = 0.2$ [Fig. 5(a)], while the contour for $\mathrm{Re}_c = 200$ does not precisely predict the boundary on the right half of the plane, it effectively anticipates both the left boundary and the turning point of the boundary. The cases on the right side of the contour of $\mathrm{Re}_c = 200$ (upper-right region), theoretically, should also exhibit a symmetric wake pattern, but it appears to be an asymmetric wake pattern. Exploring the possible reasons behind this, it may be attributed to the relatively small value of M, resulting in a lower inertia. Under the circumstances, the trajectory of the plate is prone to deflection due to disturbances. In addition, the cases in the upper-right region have relatively large values of K and θ_0, both of which are significant factors contributing to asymmetric wakes [7,13,15].

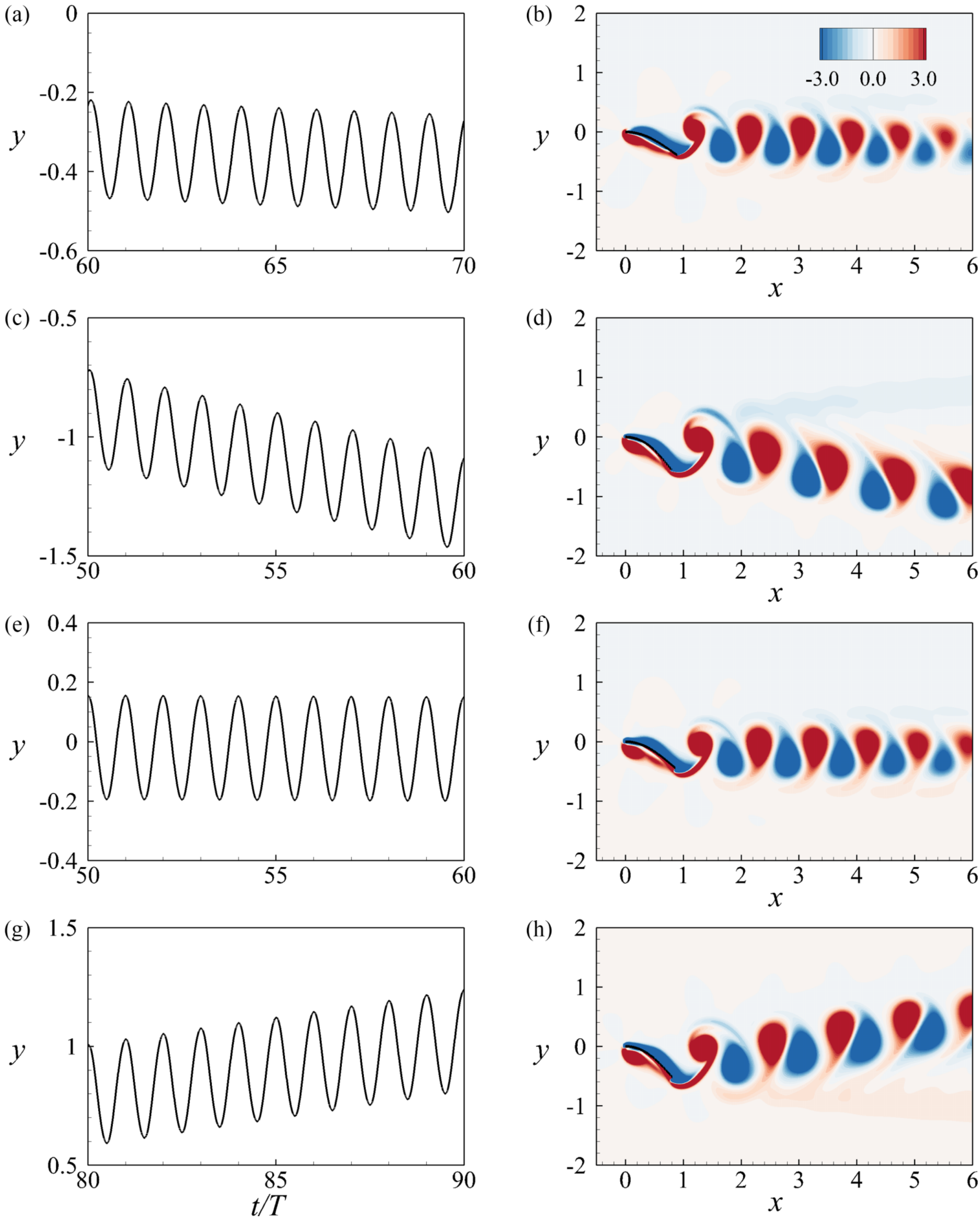

FIG. 6. Time histories of the lateral location y and the instantaneous vorticity contours for the four typical cases near the critical line, which have been marked in Fig. 5(b) ($M = 0.4$). (a), (b) Case A1: $K = 0.6$, $\theta_0 = 25^\circ$. (c), (d) Case B1: $K = 0.8$, $\theta_0 = 25^\circ$. (e), (f) Case A2: $K = 1.0$, $\theta_0 = 15^\circ$. (g), (h) Case B2: $K = 1.0$, $\theta_0 = 20^\circ$. These control parameters are also listed in Table I.

The critical values of Re_c mentioned above are denoted as $\mathrm{Re}_c^{\mathrm{cr}}$, and their corresponding contours are depicted as thick dashed lines in Fig. 5. Within the explored parameter space, asymmetric wakes appear when Re_c exceeds $\mathrm{Re}_c^{\mathrm{cr}}$. To illustrate this phenomenon, Fig. 6 shows time histories of lateral location and instantaneous vorticity contours for four representative cases close to the critical line,

TABLE I. Key parameters in cases A1, B1, A2, and B2.

Case	M	K	θ_0	Wake pattern	Re_c	U/U_{ref}	V/U_{ref}
A1	0.4	0.6	25°	Symmetric	133	0.67	0.002
B1	0.4	0.8	25°	Deflected	168	0.84	0.036
A2	0.4	1.0	15°	Symmetric	138	0.69	0.0004
B2	0.4	1.0	20°	Deflected	166	0.83	0.023

as marked in Fig. 5(b). The pertinent parameters and results of the four cases are also detailed in Table I. Notably, for cases A1 and A2, the respective Re_c values are 133 and 138, both falling below the critical threshold ($\mathrm{Re}_c^{\mathrm{cr}} = 140$). In these cases, the dimensionless lateral speed V is less than 0.01, signifying minimal lateral movement of the plates [see Figs. 6(a) and 6(e)]. Consequently, the wakes in these scenarios exhibit symmetry [see Figs. 6(b) and 6(f)]. However, slight adjustments to stiffness K or amplitude θ_0 (i.e., cases B1 and B2) lead to Re_c surpassing $\mathrm{Re}_c^{\mathrm{cr}}$ (refer to Table I). This results in a deflected trajectory and wake pattern [see Figs. 6(c), 6(d), 6(g), and 6(h)]. Hence, generally speaking $\mathrm{Re}_c^{\mathrm{cr}}$ does effectively predict wake transitions.

Our analysis now centers on $\mathrm{Re}_c^{\mathrm{cr}}$. We have seen that in Fig. 5, Re_c decreases from 200 to 65 monotonically as M increases from 0.2 to 2. To explore the possible scaling between $\mathrm{Re}_c^{\mathrm{cr}}$ and M, we plot $\mathrm{Re}_c^{\mathrm{cr}}$ against M in a log-log scale in Fig. 7(a). Further data fitting demonstrates a clear scaling relationship between $\mathrm{Re}_c^{\mathrm{cr}}$ and M:

$$\mathrm{Re}_c^{\mathrm{cr}} \sim M^{-1/2}. \tag{8}$$

This scaling can be proven through the analysis of the translational kinetic energy of the plate in the following.

The above results indicate that the wake transition depends on the propulsion speed and mass of the plate, which reminds us to examine the translational kinetic energy E_k of the plate since $E_k = (1/2)m\boldsymbol{U}^2$, where $m = \rho_l L$ is the dimensional mass of the plate. Figure 8 shows contours of dimensionless translational kinetic energy $\hat{E}_k = E_k/E_{\mathrm{ref}}$ of the plate for $M = 0.4$ and 0.8, where $E_{\mathrm{ref}} = \rho U_{\mathrm{ref}}^2 L^2$. It can be found that, similar to Re_c in Fig. 5, there is also a critical $\hat{E}_k$ (i.e., $\hat{E}_k^{\mathrm{cr}}$) separating symmetric and asymmetric wake pattern regimes in the K-θ_0 plane (see the thick dashed lines in Fig. 8). To avoid unnecessary repetition, we provide only two examples here: $M = 0.4$ and 0.8. It is noticed that the same phenomenon holds for other values of M as well. Actually, the $\hat{E}_k^{\mathrm{cr}}$ for cases with different M can be calculated from the $\mathrm{Re}_c^{\mathrm{cr}}$ (corresponding to a critical speed $|\boldsymbol{U}|^{\mathrm{cr}}$) in Fig. 5, as listed in Table II. Surprisingly, for different M, $\hat{E}_k^{\mathrm{cr}}$ is approximately the same, i.e.,

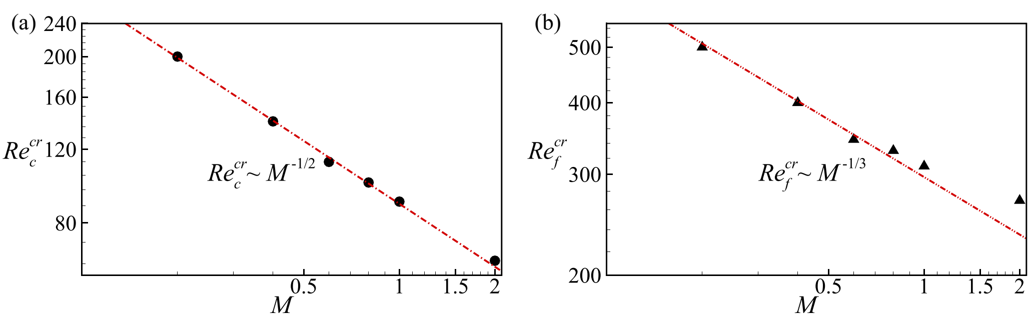

FIG. 7. (a) Critical cruising Reynolds number $\mathrm{Re}_c^{\mathrm{cr}}$ and (b) critical flapping Reynolds number $\mathrm{Re}_f^{\mathrm{cr}}$ as functions of M.

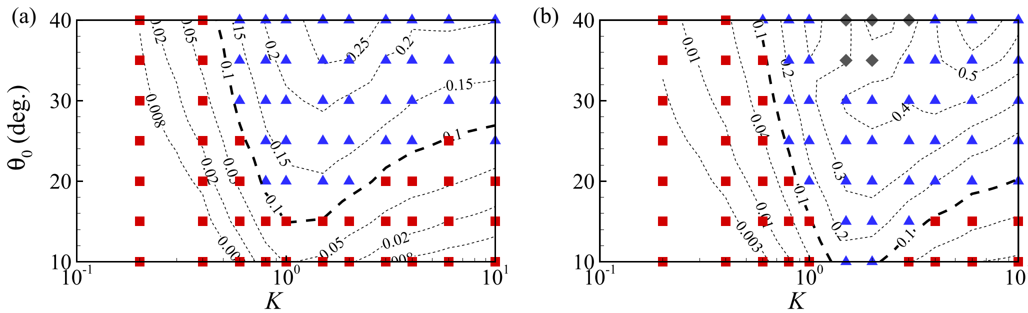

FIG. 8. Contours of the dimensionless translational kinetic energy $\hat{E}_k$ of the plate for $M = 0.4$ (a) and 0.8 (b). Symbols are identical to those in Fig. 5. The thick dashed lines correspond to the critical translational kinetic energy $\hat{E}_k^{\rm cr}$. The energy is normalized by $E_{\rm ref} = \rho U_{\rm ref}^2 L^2$.

$\hat{E}_k^{\rm cr} \approx 0.1$ (see Fig. 8 and Table II). The formula can also be written in a dimensional form as

$$E_k^{\rm cr} = C, \tag{9}$$

where $C = 0.1E_{\rm ref} = 0.1\rho U_{\rm ref}^2 L^2$. Note that the coefficient C depends on the characteristic quantities of the system, e.g., the dimensional length of the plate L. Here, in our simulation system, L is invariant since the plate is inextensible. In addition, the characteristic quantities ρ, $U_{\rm ref}$, and L are all fixed. Hence, C is a constant in our paper.

Equation (9) indicates that, once the energy (E_k) reaches a certain threshold, the symmetric wake will experience symmetry breaking. This observation aligns with the physical intuition that increased energy of a system makes it more unstable. Thus, from an energy perspective, we have a reasonable explanation for the wake transition. What is more, since $E_k^{\rm cr} = (1/2)m(\boldsymbol{U}^{\rm cr})^2 = C$, we have $|\boldsymbol{U}|^{\rm cr} \sim m^{-1/2}$. From the definitions of Re_c and M, the formula can be further written as $\mathrm{Re}_c^{\rm cr} \sim M^{-1/2}$. Hence, the scaling law (8) is well confirmed.

In the context of self-propulsion, the flapping Reynolds number $\mathrm{Re}_f = 2\pi f A_t L/\nu$ is another crucial parameter to consider [37]. Here, A_t is the amplitude of the plate's trailing edge and is determined *a posteriori* based on simulation results. Figure 9 depicts the contours of Re_f, which also reveal a critical value (denoted as $\mathrm{Re}_f^{\rm cr}$; see the thick dashed lines in Fig. 9) beyond which the wake becomes asymmetric. The behavior is similar to that of $\mathrm{Re}_c^{\rm cr}$. In previous research [21], we discovered a straightforward scaling law between Re_c and Re_f: specifically, $\mathrm{Re}_c \sim \mathrm{Re}_f^{3/2}$. This scaling indicates a one-to-one correspondence between Re_c and Re_f. Therefore, both Re_c and Re_f serve as vital indicators of wake transition. Taking into account the critical condition, i.e., $\mathrm{Re}_c^{\rm cr} \sim (\mathrm{Re}_f^{\rm cr})^{3/2}$, combined with Eq. (8), we can express the scaling law between $\mathrm{Re}_f^{\rm cr}$ and M as follows:

$$\mathrm{Re}_f^{\rm cr} \sim M^{-1/3}. \tag{10}$$

TABLE II. The critical cruising Reynolds number $\mathrm{Re}_c^{\rm cr}$, critical speed $|\boldsymbol{U}|^{\rm cr}$, and critical dimensionless translational kinetic energy $\hat{E}_k^{\rm cr}$ for various M.

M	$\mathrm{Re}_c^{\rm cr}$	$\|\boldsymbol{U}\|^{\rm cr}/U_{\rm ref}$	$\hat{E}_k^{\rm cr}$
0.2	200	1.0	0.100
0.4	140	0.7	0.098
0.6	115	0.575	0.099
0.8	100	0.5	0.100
1.0	90	0.45	0.101
2.0	65	0.325	0.106

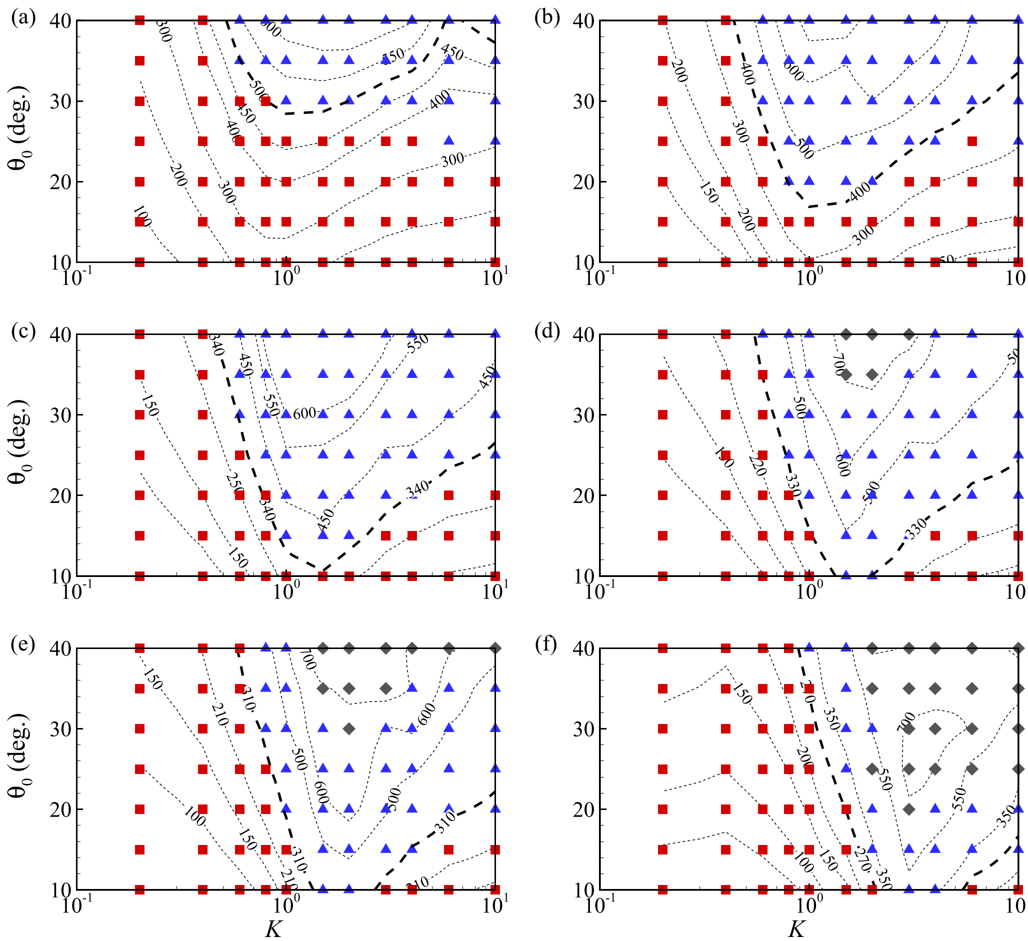

FIG. 9. Contours of the flapping Reynolds number Re_f for $M = 0.2$ (a), 0.4 (b), 0.6 (c), 0.8 (d), 1.0 (e), and 2.0 (f). Symbols are identical to those in Fig. 5. The thick dashed lines denote the critical flapping Reynolds number $\mathrm{Re}_f^{\mathrm{cr}}$.

The result is highly consistent with our observation from Fig. 7(b), where $\mathrm{Re}_f^{\mathrm{cr}}$ as a function of M is plotted. Note that, for a large M (i.e., $M = 2$), the result does not collapse well to the fitting line [Fig. 7(b)]. The potential explanation is that the scaling law $\mathrm{Re}_c \sim {\mathrm{Re}_f}^{3/2}$ might not be entirely suitable for scenarios with higher M. It is worth noting that the relationship $\mathrm{Re}_c \sim \mathrm{Re}_f^{3/2}$ is derived from cases with lower M and constraints on lateral movement [21].

B. The mechanisms of wake transitions

Next, we attempt to conduct comprehensive discussions and analyses of our results in comparison to those presented in Refs. [16,17] to explore the potential mechanisms, i.e., how being both flexible and unconstrained changes the wake.

In Ref. [16], where lateral motion is constrained, the occurrence of passive lateral oscillation and drift of the leading edge of the plate is precluded. However, when the plate is laterally unconstrained, the results exhibit significant variation. Figure 10 illustrates the plate shapes at six instants during the downstroke period for three representative cases. It is evident that the unconstrained plate undergoes substantial lateral oscillation. For instance, in the case with $K = 4$, $M = 0.4$, and $\theta_0 = 20^\circ$

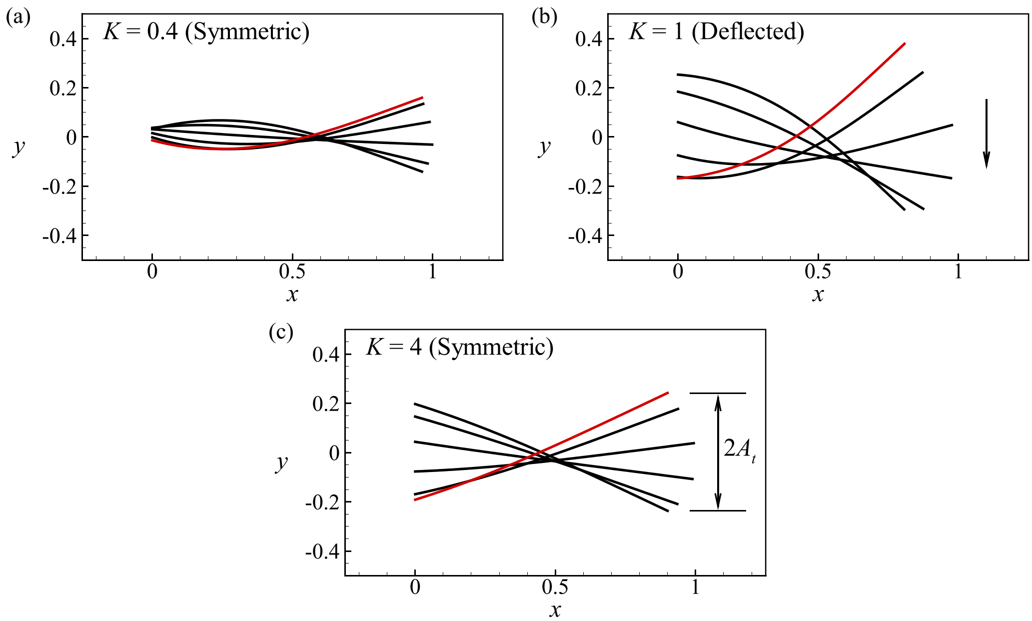

FIG. 10. Plate shapes at six instants during the downstroke period in an inertial frame moving with the plate for (a) $K = 0.4$, (b) $K = 1$, and (c) $K = 4$ with $M = 0.4$ and $\theta_0 = 20^\circ$. Here, A_t is the trailing edge amplitude of the plate.

[see Fig. 10(c)], the oscillation amplitude of the leading edge closely matches that of the trailing edge. This passive lateral oscillation has a noteworthy impact on the trailing edge amplitude (A_t) of the plate, particularly for large values of K. Specifically, for a rigid constrained plate with $\theta_0 = 20^\circ$, the expected A_t (normalized by the plate length L) is $A_t = \sin\theta_0 \approx 0.342$. In contrast, for the unconstrained plate with a significant K [e.g., $K = 4$ in Fig. 10(c)], A_t is only 0.24 [see Fig. 10(c)], representing a nearly 30% decrease. Consequently, in the case of a large K as shown in Fig. 10(c), the wake exhibits symmetry since a smaller A_t is conducive to maintaining wake symmetry, as discussed in Refs. [13,15]. This differs from the outcomes of constrained plates in Ref. [16], where the wake of a rigid plate with small M is deflected. Similar results were also observed in the study of unconstrained rigid foils in Ref. [17], where symmetry breaking of the wake was never observed. This discrepancy may be attributed to the limited amplitude range of θ_0 in their investigation, specifically, $\theta_0 \in [5^\circ, 30^\circ]$.

For cases with small or moderate K [e.g., $K = 0.4$ and 1 in Figs. 10(a) and 10(b)], the plates undergo significant bending deformations, marking a fundamental distinction between our paper and Ref. [17]. It is crucial to note that the pitching motion of the trailing edge, denoted as $\theta_t(t) = \theta_{t,0}\sin(2\pi ft + \phi_t)$ (see Fig. 1), involves the pitching amplitude $\theta_{t,0}$ and the phase difference ϕ_t between the leading and trailing edges. Due to bending deformations, $\theta_{t,0}$ deviates from θ_0.

Figure 11 presents A_t, $\theta_{t,0}$, and ϕ_t as functions of K for various θ_0 with $M = 0.4$. It is seen that for a fixed θ_0, as K increases, both A_t and $\theta_{t,0}$ initially increase and then decrease, reaching their peaks at a moderate K [see Figs. 11(a) and 11(b)]. This phenomenon occurs because, with small K, the phase difference ϕ_t approaches 180° [see Fig. 11(c)], indicating nearly antiphase pitching motions of the leading and trailing edges. Consequently, $\theta_{t,0}$ is smaller than the active motion amplitude θ_0 [see Fig. 11(b)], resulting in a symmetric wake (see Fig. 5).

As K increases, ϕ_t monotonically decreases [see Fig. 11(c)]. At moderate K, $\theta_{t,0}$ can significantly surpass θ_0 due to bending deformations. For example, at $K = 1.5$ and $M = 0.4$, $\theta_{t,0} = 35.7^\circ$ when $\theta_0 = 20^\circ$, and $\theta_{t,0} = 64^\circ$ when $\theta_0 = 40^\circ$ [see Fig. 11(b)]. In other words, appropriate flexibility

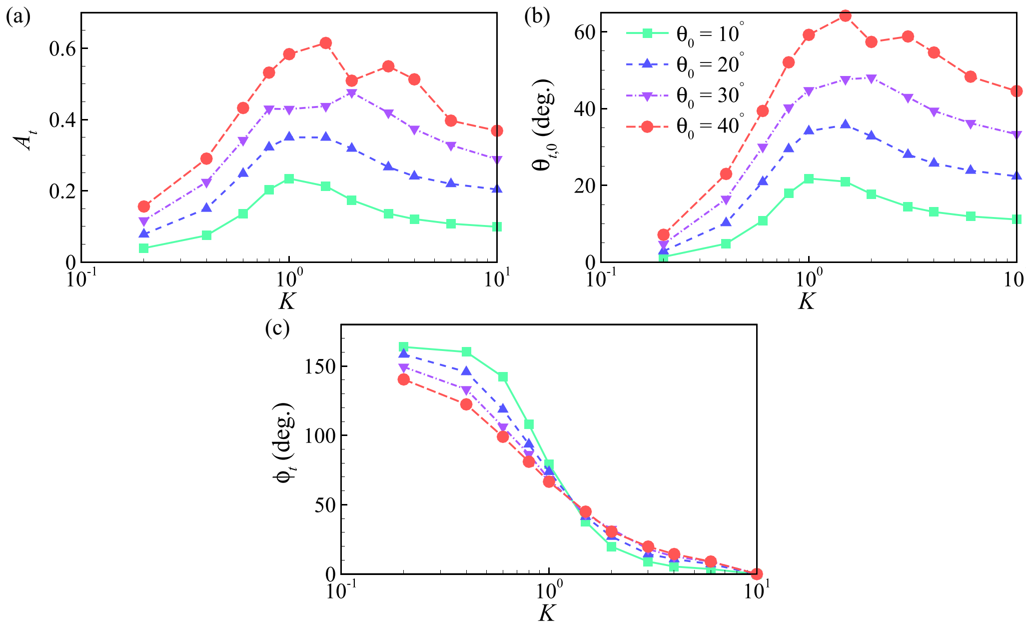

FIG. 11. (a) The trailing edge amplitude A_t, (b) the pitching amplitude of the trailing edge $\theta_{t,0}$, and (c) the phase difference ϕ_t between the pitching motions of the leading and trailing edges as functions of K for various θ_0 with $M = 0.4$.

can substantially amplify the trailing edge amplitude, tending to result in asymmetric wakes. In addition, larger flapping amplitude means that the plate may generate larger thrust and be propelled faster [17,21]. Therefore, the maximum propulsion speed is achieved at moderate K, as shown in Fig. 4.

For large K, ϕ_t approaches zero [see Fig. 11(c)], and the bending deformation becomes minimal [see Fig. 10(c)]. Consequently, under these circumstances, $\theta_{t,0}$ approximates θ_0 [see Fig. 11(b)].

Based on the above analysis, two distinct mechanisms emerge as influential factors shaping the wake symmetry properties of unconstrained flexible plates. The first mechanism involves passive lateral oscillation, which serves to diminish the trailing edge amplitude (A_t or $\theta_{t,0}$), thereby mitigating the potential for symmetry breaking. The second mechanism is associated with passive bending deformation, contributing to the variability in A_t or $\theta_{t,0}$—whether augmentation or reduction—depending on the value of K.

It is noteworthy that in Ref. [17] the unconstrained foil is rigid, whereas in Ref. [16] the flexible plate is constrained. Consequently, in their respective studies, only one of these mechanisms was at play. In contrast, our paper incorporates both mechanisms, significantly distinguishing our results from theirs.

To better illustrate significant differences in wake asymmetry development among various constrained situations, i.e., the fixed, laterally constrained, and unconstrained scenarios, we have generated quantitative maps for wake asymmetry in the fixed and laterally constrained situations (as a function of K and θ_0), as shown in Fig. 12. In the fixed situation, the oncoming flow speed equals the propulsion speed of the unconstrained plate with the same K and θ_0. Additionally, for comparison, we have included the boundary for the unconstrained cases depicted with dashed black lines, corresponding to the critical line presented in Fig. 5(b).

Figure 12(a) reveals that, when $K > 3$, even with a small pitching angle θ_0 (e.g., $\theta_0 = 10^\circ$), the fixed situation exhibits an asymmetric wake compared to the unconstrained situation [as observed

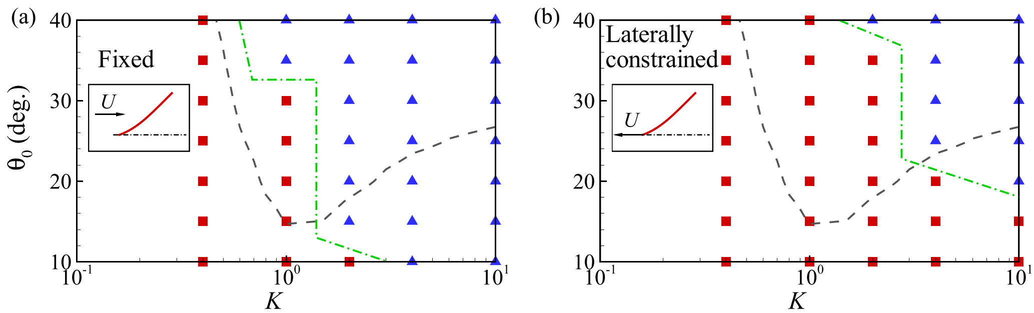

FIG. 12. Wake pattern regimes in the (K, θ_0) plane are illustrated for both the (a) fixed and (b) laterally constrained plate with $M = 0.4$. The green dash-dotted lines serve as indicators of the boundary between symmetric (□) and asymmetric (△) regimes for each situation. Additionally, for reference, the boundary for the unconstrained cases is depicted with dashed black lines, derived from the critical line presented in Fig. 5(b).

in the lower right part of the (K, θ_0) plane]. This confirms that the lateral oscillation motion of the unconstrained plate can indeed suppress the symmetry breaking of the wake, as discussed above.

For the laterally constrained situation [see Fig. 12(b)], the border between symmetric and asymmetric moves rightward compared to the unconstrained situation (dashed black line). At moderate K (e.g., $K = 1$), the amplitude of the unconstrained plate is larger [see Fig. 11(a)], and the lateral unconstrained characteristic makes the movement direction of the plate more prone to tilting, resulting in a deflected (asymmetric) wake. These once again elucidate the pivotal role of unconstrained scenarios and flexibility of the plate.

V. CONCLUSIONS

In this paper, we conduct a numerical investigation to examine the wake symmetry properties of an unconstrained flexible plate, capable of longitudinal and lateral movement. Our analysis identifies three distinct wake patterns: symmetric, deflected asymmetric, and chaotic asymmetric. The lateral drift speed (V) serves as a quantitative indicator, distinguishing between these wake patterns. Symmetric cases exhibit minimal lateral drift, while asymmetric cases display comparatively higher values of V. Our results suggest that symmetry breaking within the symmetric wake occurs when Re_c reaches a critical threshold ($\mathrm{Re}_c^{\mathrm{cr}}$), provided that M is not too small. Remarkably, we observe a straightforward scaling relationship between $\mathrm{Re}_c^{\mathrm{cr}}$ and the mass ratio (M), described as $\mathrm{Re}_c^{\mathrm{cr}} \sim M^{-1/2}$. Furthermore, we find that the critical translational kinetic energy of the plate (E_k^{cr}) remains constant across different M values when wake transitions occur, i.e., $E_k^{\mathrm{cr}} = C$. By scrutinizing the translational kinetic energy (E_k), we can demonstrate our scaling of $\mathrm{Re}_c^{\mathrm{cr}}$. We also establish a scaling relationship for the critical flapping Reynolds number ($\mathrm{Re}_f^{\mathrm{cr}}$), which scales as $\mathrm{Re}_f^{\mathrm{cr}} \sim M^{-1/3}$. This scaling is derived from the Re_c scalings observed in this paper and in prior research. Lastly, two key mechanisms affecting wake symmetry properties are revealed. Specifically, the passive lateral oscillation can reduce the trailing edge amplitude (A_t or $\theta_{t,0}$), which is beneficial for suppressing the symmetry breaking of the wake, while the bending deformation can either augment or reduce A_t (or $\theta_{t,0}$), depending on the value of K, thus having different effects on the wake structures. We have also generated quantitative maps for wake symmetry properties in different constrained situations to further illustrate the significant effects of flexibility and unconstrained characteristic of the plate.

Note that in the present paper Re is relatively low (Re = 200). If Re is large, the scaling relations mentioned above may be different. These findings may contribute to a deeper understanding of biological swimming and flying locomotion, providing valuable insights for bionic design and engineering applications.

ACKNOWLEDGMENTS

Some of the calculations were performed at the Supercomputing Center of the University of Science and Technology of China. This work was supported by National Natural Science Foundation of China Grants No. 11972342 and No. 11772326.

[1] T. Wu, Fish swimming and bird/insect flight, Annu. Rev. Fluid Mech. **43**, 25 (2011).
[2] G. Lauder, Fish locomotion: Recent advances and new Directions, Annu. Rev. Mar. Sci. **7**, 521 (2015).
[3] M. Triantafyllou, G. Triantafyllou, and D. Yue, Hydrodynamics of fishlike swimming, Annu. Rev. Fluid Mech. **32**, 33 (2000).
[4] A. Smits, Undulatory and oscillatory swimming, J. Fluid Mech. **874**, P1 (2019).
[5] A. Andersen, T. Bohr, T. Schnipper, and J. H. Walther, Wake structure and thrust generation of a flapping foil in two-dimensional flow, J. Fluid Mech. **812**, R4 (2017).
[6] N. Lagopoulos, G. Weymouth, and B. Ganapathisubramani, Universal scaling law for drag-to-thrust wake transition in flapping foils, J. Fluid Mech. **872**, R1 (2019).
[7] Z.-R. Peng, Y. Sun, D. Yang, Y. Xiong, L. Wang, and L. Wang, Scaling laws for drag-to-thrust transition and propulsive performance in pitching flexible plates, J. Fluid Mech. **941**, R2 (2022).
[8] J. Zhang, Footprints of a flapping wing, J. Fluid Mech. **818**, 1 (2017).
[9] G.-J. Li and X.-Y. Lu, Force and power of flapping plates in a fluid, J. Fluid Mech. **712**, 598 (2012).
[10] D. Floryan, T. V. Buren, and A. Smits, Swimmers' wake structures are not reliable indicators of swimming performance, Bioinspir. Biomim. **15**, 024001 (2020).
[11] K. D. Jones, C. M. Dohring, and M. F. Platzer, Experimental and computational investigation of the Knoller-Betz effect, AIAA J. **36**, 1240 (1998).
[12] G. Lewin and H. Haj-Hariri, Modelling thrust generation of a two-dimensional heaving airfoil in a viscous flow, J. Fluid Mech. **492**, 339 (2003).
[13] R. Godoy-Diana, J.-L. Aider, and J. Wesfreid, Transitions in the wake of a flapping foil, Phys. Rev. E **77**, 016308 (2008).
[14] D. Cleaver, Z. Wang, and I. Gursul, Bifurcating flows of plunging aerofoils at high Strouhal numbers, J. Fluid Mech. **708**, 349 (2012).
[15] C. Marais, B. Thiria, J. Wesfreid, and R. Godoy-Diana, Stabilizing effect of flexibility in the wake of a flapping foil, J. Fluid Mech. **710**, 659 (2012).
[16] X. Zhu, G. He, and X. Zhang, How flexibility affects the wake symmetry properties of a self-propelled plunging foil, J. Fluid Mech. **751**, 164 (2014).
[17] X. Lin, J. Wu, and T. Zhang, Self-directed propulsion of an unconstrained flapping swimmer at low Reynolds number: hydrodynamic behaviour and scaling laws, J. Fluid Mech. **907**, R3 (2021).
[18] C.-K. Kang, H. Aono, C. Cesnik, and W. Shyy, Effects of flexibility on the aerodynamic performance of flapping wings, J. Fluid Mech. **689**, 32 (2011).
[19] D. Quinn, G. Lauder, and A. Smits, Scaling the propulsive performance of heaving flexible panels, J. Fluid Mech. **738**, 250 (2014).
[20] D. Floryan and C. Rowley, Clarifying the relationship between efficiency and resonance for flexible inertial swimmers, J. Fluid Mech. **853**, 271 (2018).
[21] K. Liu, X. Liu, and H. Huang, Scaling the self-propulsive performance of pitching and heaving flexible plates, J. Fluid Mech. **936**, A9 (2022).
[22] L. Zhu and C. Peskin, Simulation of a flapping flexible filament in a flowing soap film by the Immersed Boundary method, J. Comput. Phys. **179**, 452 (2002).
[23] B. Connell and D. Yue, Flapping dynamics of a flag in a uniform stream, J. Fluid Mech. **581**, 33 (2007).
[24] R.-N. Hua, L. Zhu, and X.-Y. Lu, Locomotion of a flapping flexible plate, Phys. Fluids **25**, 121901 (2013).
[25] J. Doyle, *Nonlinear Analysis of Thin-Walled Structures: Statics, Dynamics, and Stability* (Springer, New York, 2001).

[26] H. Huang, H. Wei, and X.-Y. Lu, Coupling performance of tandem flexible inverted flags in a uniform flow, J. Fluid Mech. **837**, 461 (2018).
[27] C. Zhang, H. Huang, and X.-Y. Lu, Effect of trailing-edge shape on the self-propulsive performance of heaving flexible plates, J. Fluid Mech. **887**, A7 (2020).
[28] X. Zhu, G. He, and X. Zhang, Flow-mediated interactions between two self-propelled flapping filaments in tandem configuration, Phys. Rev. Lett. **113**, 238105 (2014).
[29] M. Gazzola, M. Argentina, and L. Mahadevan, Scaling macroscopic aquatic locomotion, Nat. Phys. **10**, 758 (2014).
[30] K. Lucas, N. Johnson, W. Beaulieu, E. Cathcart, G. Tirrell, S. Colin, B. Gemmell, J. Dabiri, and J. Costello, Bending rules for animal propulsion, Nat. Commun. **5**, 3293 (2014).
[31] K. Liu, H. Huang, and X.-Y. Lu, Hydrodynamic benefits of intermittent locomotion of a self-propelled flapping plate, Phys. Rev. E **102**, 053106 (2020).
[32] Z.-R. Peng, H. Huang, and X.-Y. Lu, Collective locomotion of two closely spaced self-propelled flapping plates, J. Fluid Mech. **849**, 1068 (2018).
[33] D. Cleaver, I. Gursul, D. Calderon, and Z. Wang, Thrust enhancement due to flexible trailing-edge of plunging foils, J. Fluids Struct. **51**, 401 (2014).
[34] I. Gursul and D. Cleaver, Plunging oscillations of airfoils and wings: Progress, opportunities, and challenges, AIAA J. **57**, 3648 (2019).
[35] I. Gursul, D. Cleaver, and Z. Wang, Control of low Reynolds number flows by means of fluid–structure interactions, Prog. Aerosp. Sci. **64**, 17 (2014).
[36] S. Heathcote and I. Gursul, Jet switching phenomenon for a periodically plunging airfoil, Phys. Fluids **19**, 027104 (2007).
[37] N. Vandenberghe, J. Zhang, and S. Childress, Symmetry breaking leads to forward flapping flight, J. Fluid Mech. **506**, 147 (2004).